

A Terahertz Bandpass Filter Using a Capacitive Transition Circuit and a Spoof Surface Plasmon Polariton Waveguide

Mohsen Haghghat^{1,2} · Levi Smith^{1,2,*}

Received: date / Accepted: date

Abstract This paper presents a novel terahertz (THz) bandpass filter (BPF) based on a spoof surface plasmon polariton (SSPP) waveguide with a center frequency of 1 THz and a 3 dB bandwidth of 0.3 THz. The proposed BPF comprises cascaded high-pass and low-pass elements. The high-pass element is a capacitive gap in the SSPP transition circuit, and the low-pass element is the SSPP waveguide itself. We find that the measurement results, including cut-off frequencies, align well with the theoretical predictions and simulations. To the authors' knowledge, the proposed SSPP BPF is the first of its kind.

Keywords Terahertz · Coplanar Strip · Spoof Surface Plasmon Polaritons · BandPass Filter · Thin Membrane · Silicon Nitride

1 Introduction

Spoof surface plasmon polaritons (SSPP) devices operating at microwave and terahertz (THz) frequencies have attracted notable research attention [1–3], mainly due to their inheritable capabilities from typical surface plasmon polaritons (SPP), such as significant surface field confinement and dispersion properties which can be customized through geometric modifications [4,5]. SSPP structures were initially introduced using 3D geometries like an array of holes or grooves in a piece of metal that interacted with incident oblique light or waves [1,2]. Since then, the use of guided waves for SSPP excitation has been pursued due to their improved integration capabilities [3]. A common guided-wave SSPP waveguide consists of a corrugated single-conductor that requires a matching or transition circuit. The majority of the literature focuses on the integration of SSPP in coplanar waveguides (CPW) [6–11] due to compatibility with standard vector network analyzer probes. This involves connecting the CPW signal line to the SSPP and flaring the ground lines as the SSPP stub length increases gradually [9]. This configuration requires large areas of flaring ground planes in the transition circuit (TC), which consumes the area of the chip [9].

An SSPP waveguide can consist of more than one conductor; an example is the CPS-SSPP waveguide, where corrugations are introduced in each conductor of a standard CPS [12–14]. An important benefit

1. Department of Electrical and Computer Engineering, University of Victoria, Victoria, BC V8P 5C2, Canada.

2. Centre for Advanced Materials and Related Technology (CAMTEC), University of Victoria, 3800 Finnerty Rd, Victoria, BC V8P 5C2, Canada.

* Corresponding author; E-mail: levismith@uvic.ca

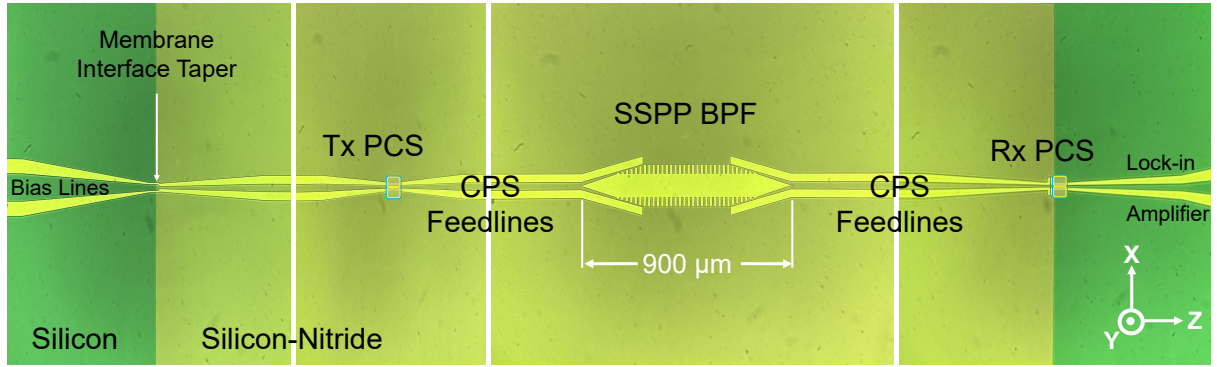


Fig. 1: Fabricated THz SSPP BPF on thin Si-N membrane with CPS feedlines and transition circuits for excitation and Tx/Rx PCS for THz generation and detection.

of the CPS-SSPP is the ease of integration with CPS feedlines that can be excited by photoconductive switching, which allows the investigation of devices at THz frequencies [1]. Like single-conductor SSPP waveguides, the transmission characteristics of a typical CPS-SSPP waveguide exhibit low-pass behavior that can be adjusted by the corrugation geometry. In this work, this low-pass behavior is used to control the upper-cut frequency of the BPF. Next, exciting the SSPP mode requires a TC. For the CPS-SSPP the TC consists of a gradual ramp in the corrugation depth. This work has a unique TC that interconnects a CPS feedline with a single-conductor SSPP waveguide. The combination of the TC and the SSPP waveguide forms the proposed BPF.

The majority of the SSPP literature is focused on SSPP waveguiding with low loss throughout a limited bandwidth, such as [7] or showing its low-pass filtering due to slow-wave properties such as [15]. SSPP-based band-pass filters (BPF) have been reported in limited numbers at microwave and mm-wave frequencies [16–20]; however, these structures generally use microwave cavities, which are difficult to integrate on a chip. In addition, there is a lack of experimentally validated SSPP-based BPF research at THz frequencies, mainly due to the lack of equipment and waveguiding challenges, such as different sources of loss at these frequencies [3, 21].

This paper presents the experimental demonstration of a novel THz SSPP-based BPF structure by introducing the integration of CPS feedlines into a single conductor SSPP for the first time. It has been presented with simulation in our preliminary work at the 300 GHz band [22]. For the integration of SSPP to CPS, a transition circuit (TC) is proposed to convert the quasi-TEM mode of the CPS to the SSPP TM mode [9, 14]. This is achieved by gradually extending the length of SSPP stubs while tapering the CPS lines and eventually terminating the CPS conductors. This TC configuration couples the propagating wave to the SSPP and blocks the low frequencies. To operate at THz frequencies, we employed a thin 1 μm silicon nitride (SiN) membrane, which mitigates loss and dispersion at THz frequencies [14, 23]. Figure 1 illustrates the proposed SSPP-based bandpass filter fabricated on the SiN membrane, together with photo-conductive switches (PCS) for THz generation and detection. Figure 2 shows the cross-section of the CPS feedlines on the SiN membrane.

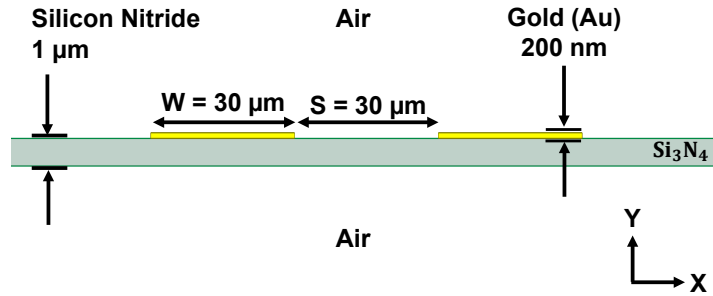


Fig. 2: Cross section of CPS feedlines on the thin Silicon Nitride membrane.

Table 1: Stub lengths for the TC (Units: μm)

H_n	H_1	H_2	H_3	H_4	H_5	H_6
35	5	10	15	20	25	30
42	6	12	18	24	30	36
49	7	14	21	28	35	42

2 Design and Simulation

ANSYS HFSS was used to assist in the design process and also to simulate the designed structure. Specifically, eigenmode simulations were used to obtain the dispersion curves for the SSPP waveguide unit cell. Frequency-domain (FD) simulations were also used to obtain the frequency-dependent S-parameters for the BPF. The simulated constitutive material parameters are as follows: $\epsilon_{r,\text{SiN}} = 7.6$, $\sigma_{\text{SiN}} = 0$ and $\tan \delta_{\epsilon,\text{SiN}} = 0.00526$ [24], and for the conductors $\sigma_{\text{Au}} = 4.1 \times 10^7$ S/m or $\sigma_{\text{cond}} = \infty$ depending on the simulation. For all simulations, the thickness of the SiN substrate is $1 \mu\text{m}$ and the conductor thickness is 200 nm .

The BPF presented in this work is a proof of concept selected to operate at THz frequencies. For this purpose, we select a center frequency of 1 THz and a bandwidth of 0.3 THz . For the design procedure, the BPF can be divided into cascaded low-pass and high-pass elements that are mostly independent of each other. The BPF consists of a single-conductor SSPP waveguide with a tapered CPS transition circuit (TC) as shown in Figure 3. The TC acts as a high-pass filter and also performs mode conversion between the CPS TEM mode and the SSPP TM mode. The high-pass behavior is achieved using the capacitive gap between the CPS and the single-conductor SSPP waveguide. Mode conversion is achieved by gradually increasing the length of single-conductor SSPP stubs within the TC [6, 14]. The lengths of the stubs are linearly tapered and tabulated in Table 1, where the row in bold font is a fabricated structure used in the experiment.

The upper cut-off frequency is controlled by the dimensions of the SSPP waveguide, in particular the heights of the stubs, H_n . We used an eigenmode simulation on the SSPP unit cell to extract the dispersion curves and the band-edge frequencies. Figure 4 plots the results of an eigenmode simulation for the unit cell shown in the inset. In this simulation, the period $d = 20 \mu\text{m}$, the aperture $a = 10 \mu\text{m}$, and the width of the central conductor, $W_0 = 90 \mu\text{m}$, were fixed, and H_n was varied to obtain the different

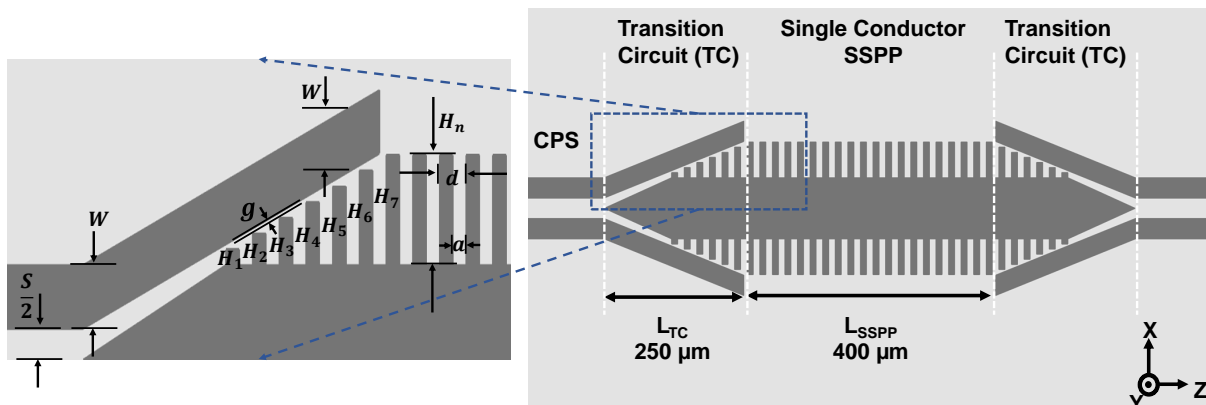


Fig. 3: CPS to SSPP transition circuit dimensions for the proposed BPF

curves. We selected a subwavelength value for d and a as they must be much smaller than the wavelength [2, 25, 26]. From Fig. 4, it is clear that the band-edge frequency associated with $k_z d = \pi$ depends on H_n . In short, small values of H_n correspond to higher values for the upper cut-off frequency. We note that the solid (red) trace in Fig. 4 corresponds to the fabricated structure.

The upper cut-off frequency can also be calculated by an analytical dispersion expression assuming that the SSPP shown in Fig. 3 is modeled like a symmetric (y - z plane) 1D array of grooves with finite thickness by [2, 26]:

$$k_z = k_{eff} \sqrt{1 + (a/d)^2 \tan^2(k_{eff} H_n)}, \quad (1)$$

where $k_{eff} = \omega \sqrt{\epsilon_{eff}} / c$ is the effective wavenumber, c is the speed of light, and ϵ_{eff} is the effective relative permittivity which depends on H_n . From simulations, an SSPP waveguide on a thin SiN membrane, the effective permittivity can be approximated by $\epsilon_{eff} = 2.15, 2.0, 1.85$ when $H_n = 35, 42, 49$ μm , respectively. Similarly to Fig. 4, the solution to (1) shows that the band edge (and the associated upper cutoff frequency) of the SSPP structures are primarily controlled by H_n , thus (1) provides a useful starting point and theoretical aid in the design of SSPP filters [6, 15]. However, we recommend that numerical eigenmode simulations be used prior to actual device fabrication, as they provide a more accurate prediction of device performance. Lastly, we note that the solution to (1) for $H_n = 42$ μm predicts an upper cut-off frequency of 1.2 THz.

We used a 1 μm thick SiN substrate, which has been selected to minimize loss and dispersion [23]; however, other substrates can be used to implement this structure, expecting higher loss at THz frequencies. Note that using other substrates changes the effective permittivity and the band-edge locations; hence, the relation between the geometry and the band-edge should be recalculated.

The lower cut-off frequency is determined primarily by the gap between the tapered CPS feedlines and the single-conductor SSPP in the TC, which is indicated as g in Fig. 3. Reducing the gap between the tapered CPS and TC stubs increases the series capacitance, thereby reducing the lower cut-off frequency. In contrast, increasing the gap decreases the capacitance, which increases the lower cut-off frequency. However, increasing the gap also reduces the coupling and increases the insertion loss. We selected $g = 4$ μm to have an acceptable passband insertion loss (IL), which was found to be ≈ 1.5 dB from simulation and a bandwidth of 0.3 THz. Another method of controlling the lower cut-off frequency is to increase

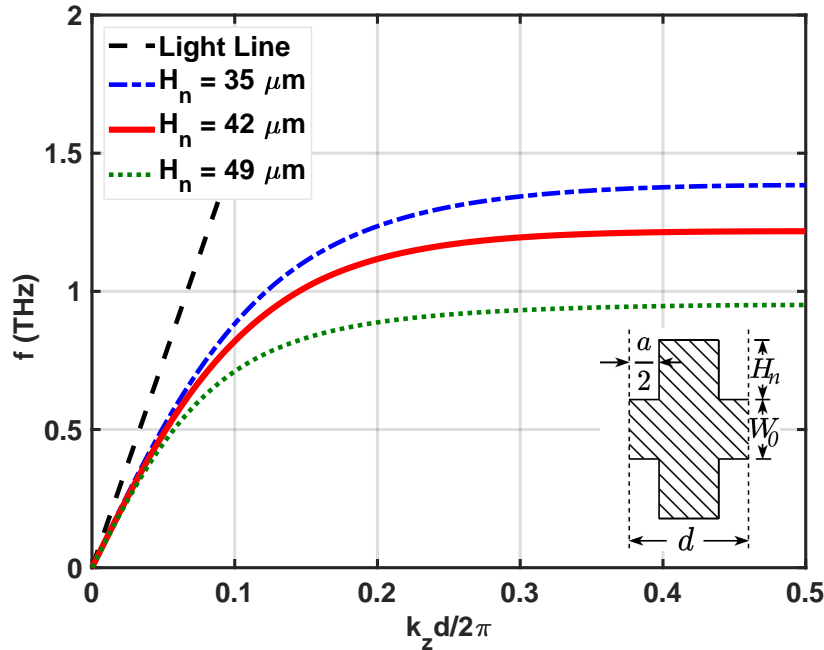


Fig. 4: BPF Unit Cell Dispersion Curves, determining upper cut-off frequency. Unit cell dimensions: $d = 20 \mu\text{m}$, $a = 10 \mu\text{m}$, $W_0 = 90 \mu\text{m}$, $21 \mu\text{m} \leq H_n \leq 70 \mu\text{m}$.

the length of the TC coupling region. This is denoted as L_{TC} in Fig. 3. Larger values of L_{TC} will enable wider bandwidths.

As mentioned, the objective of the proposed filter is to combine low-pass and high-pass responses to produce a BPF by integrating the CPS feedlines, the TCs and the single-conductor SSPP waveguide, as shown in Fig. 3. To predict the broadband response of the BPF numerical simulations should be used. First, we look at the transmission response for different values of H_n when the conductors are modeled as PECs. The result is plotted in Fig. 5. For these simulations, $d = 20 \mu\text{m}$, $a = 10 \mu\text{m}$, $S = 30 \mu\text{m}$, and $W = 30 \mu\text{m}$. From Fig. 5 it is clear that the upper cut-off frequency is dependent on the value of H_n which is aligned with the results of the eigenmode simulation for the unit cell plotted in Fig. 4.

Next, we model the 200 nm thick conductors as gold to observe the effect of a finite conductivity. The S-parameters for the BPF are shown in Fig. 6 which illustrates a passband insertion loss of 5-7 dB.

For visualization of filter operation, Fig. 7 illustrates the electric field plots for the structure with $H_n = 42 \mu\text{m}$ at 1 THz in the passband and lower/upper stopbands at 0.5 and 1.5 THz. The field plot at 1 THz also illustrates the field confinement capability of the SSPP structure in the groove areas.

3 Experiment

The experimental setup for the measurements is a modified THz time-domain spectroscopy (THz-TDS) setup presented in [23], as depicted in Fig. 8. This setup utilizes a femtosecond pulsed laser with specific

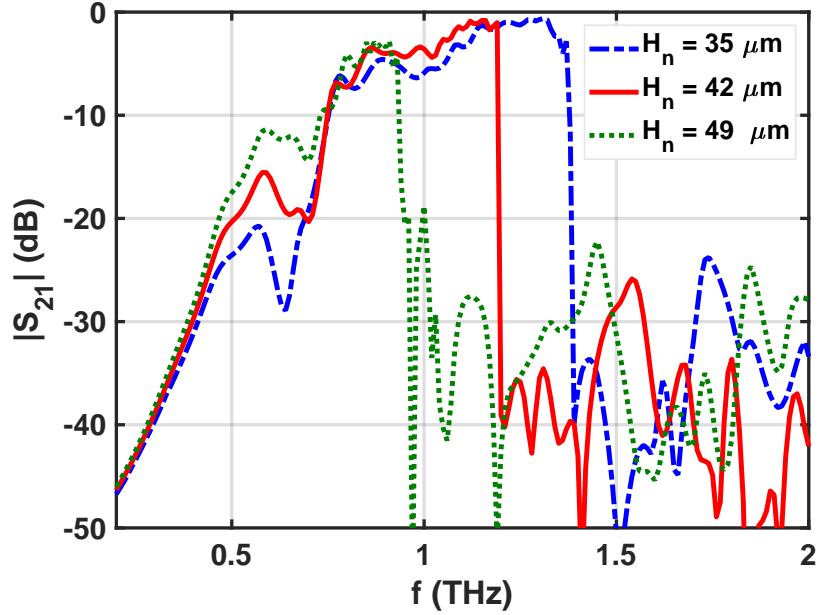


Fig. 5: Transmission response (S_{21}) of the SSPP BPF structure with variable H_n from 28 μm to 70 μm when the conductor is modeled as PEC.

parameters: a wavelength of 780 nm, a pulse width of 90 fs, a pulse rate of 80 MHz, and an average output power of 27 mW. The laser beam is focused onto the photoconductive switches (PCS) placed on the designated transmitter (Tx) and receiver (Rx) spots on the feedlines (see Fig. 1), serving as transmitter and receiver, to generate and detect THz pulses with photoconductive switching and sampling methods [23].

The PCS, with dimensions of 70 $\mu\text{m} \times 40 \mu\text{m} \times 1.5 \mu\text{m}$ and a 5 μm gap between the metal contacts of the PCS (gold), are bonded using water droplets with Van der Waals forces (VDW), as explained in [27]. The transmitted signal is then reconstructed by adjusting a mechanical delay line and measuring the receiver current using a lock-in amplifier, following techniques similar to those employed in conventional THz-TDS setups [23, 28].

The fabrication of photo-conductive switches (PCSs) involves a multi-step process. Initially, a low-temperature grown gallium arsenide (LT-GaAs) layer is deposited on a sacrificial aluminum arsenide (AlAs) layer, which is situated on a semi-insulating GaAs substrate. Subsequently, the LT-GaAs surface undergoes photolithography to establish Au contacts. Each PCS region is then masked and subjected to wet etching using citric acid and hydrogen peroxide to define the PCS thickness. After cleaning and re-masking with etch-resist wax, the LT-GaAs layer is dissolved in hydrofluoric acid (HF), separating it from the AlAs layer. Additional steps are taken to disconnect the remaining LT-GaAs film, resulting in the formation of multiple active regions of LT-GaAs PCSs [29].

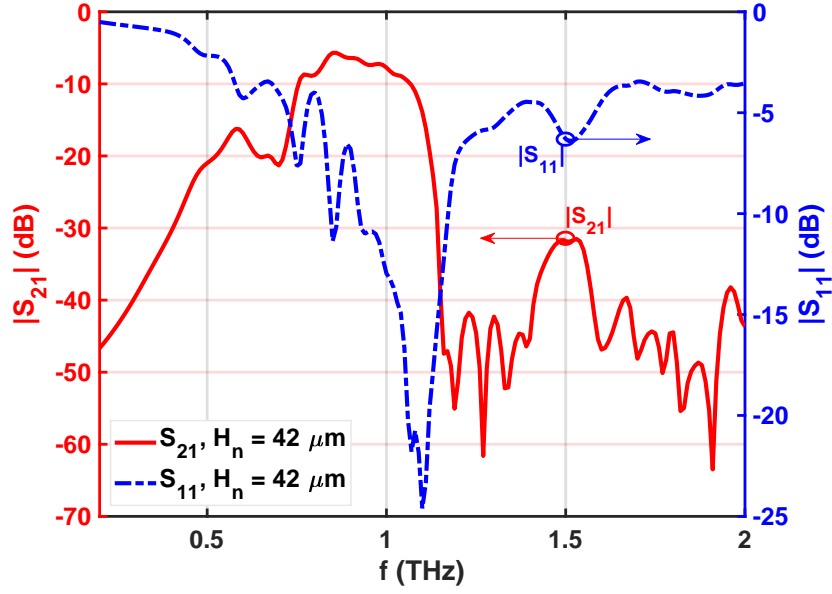


Fig. 6: S_{21} and S_{11} of the BPF structure with $H_n = 42 \mu\text{m}$ considering dielectric and conductor losses.

4 Measurement Results and Discussion

The experimental results of a reference CPS waveguide and SSPP-based BPF with $H_n = 42 \mu\text{m}$ are shown in Fig. 9(a,b). The reference CPS is a feedline shown in Fig. 1 of the same length. The temporal response of CPS is a transient subpicosecond pulse (Fig. 9a) that will have a broad spectral content. For the BPF, the temporal response is oscillatory (Fig. 9b), aligned with a narrow-band signal. As expected, the oscillation period is ≈ 1 ps which corresponds to 1 THz, which is the center frequency of the BPF device under test. Figure 9c displays the corresponding spectral responses obtained by applying the Discrete Fourier Transform (DFT) to the temporal responses. The spectral response of the BPF shows sharp reductions at 0.8 and 1.2 THz, which are aligned with the simulated predictions shown in Fig. 6.

The comparison of spectral responses in Fig. 9 shows 15-20 dB out-of-band rejection for BPF, which is lower than expected, which should be more than 20 dB for low frequencies and more than 30 dB for upper band rejection. This is primarily because of noise levels and the weakness of the BPF output since it is a relatively narrow-band signal and holds only a small portion of the total pulse energy. Thus, the low signal-to-noise ratio disrupts the resolution of the real out-of-band rejection of the filter. Despite the weakness of the signal power, the measured out-of-band rejection is acceptable. Another important parameter to be extracted from the measurement results is the difference between the amplitude of the spectrum between the BPF and CPS reference in the passband, which is ≈ 5 dB that aligns with the minimum insertion loss expectations from the S-parameter simulations (see Fig. 6).

We also compared the simulated S_{21} with the measured pulse normalized to the simulated passband transmission to illustrate the operation of the device in Fig. 10. Comparison between simulated and

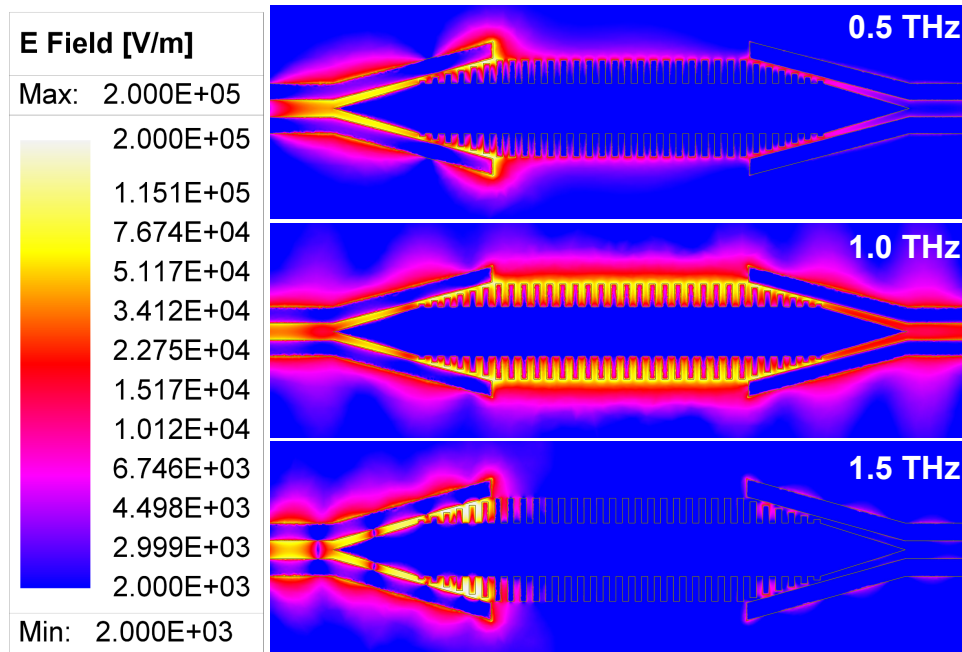


Fig. 7: Field plots of the proposed SSPP BPF structure with $H_n = 42 \mu\text{m}$ at 0.5 THz (lower stopband), 1 THz (passband), and 1.5 THz (upper stopband). The temperature (color) scale ranges from blue (2×10^3 V/m) to white (2×10^5 V/m) on a logarithmic scale.

experimental spectral responses shows reasonable agreement and demonstrates that our proof-of-concept filter is a promising candidate for future THz BPFs.

It is worth mentioning that the spectral responses have inherent amplitude decay because these are Fourier transforms of finite-duration transient pulses rather than impulses with a flat spectrum [14, 23]. Therefore, the spectrum of BPF has a baseline that resembles the reference spectral curve. The fluctuations in the measurement are attributed to uncorrelated system noise sources, including those from the laser, equipment, and environment, as well as fluctuations in the PCS photo-current due to fabrication imperfections. These effects were also observed in the measurement of the CPS reference, where we expect a much smoother spectral response based on simulations.

5 Conclusion

This paper introduces a novel terahertz (THz) spoof surface plasmon polariton (SSPP) bandpass filter, marking a significant milestone in SSPP-based filter structures by integrating a single-conductor SSPP to CPS. Through experimental validation, the filter demonstrates impressive performance metrics, including a low passband amplitude difference of 5 dB compared to a CPS feedline with the same length and dimensions, and out-of-band rejection surpassing 20 dB for low frequencies and about 15-20 dB for high frequencies. With a 3 dB bandwidth of approximately 0.3 THz, ranging from 0.87 to 1.17 THz, the filter exhibits robust signal transmission and rejection capabilities within its passband and stopbands, closely

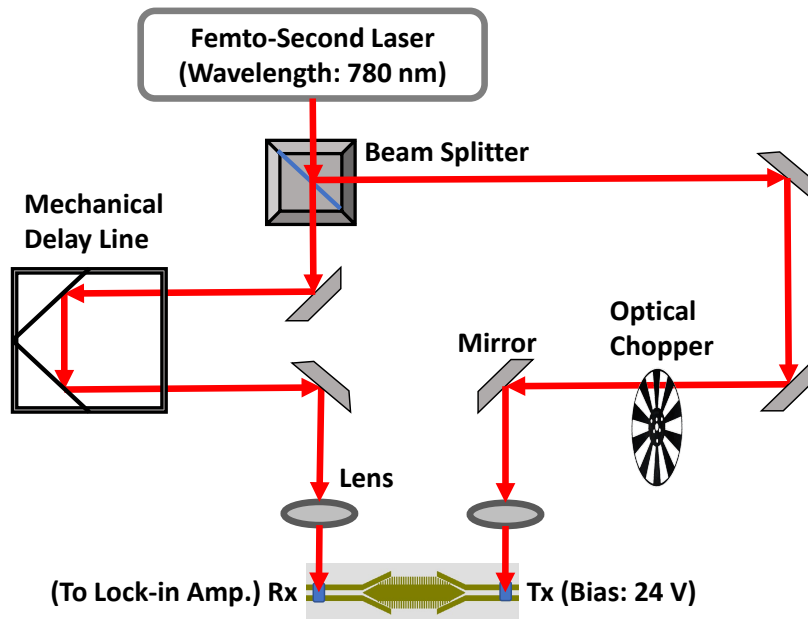


Fig. 8: BPF measurement setup based on modified THz time domain spectroscopy

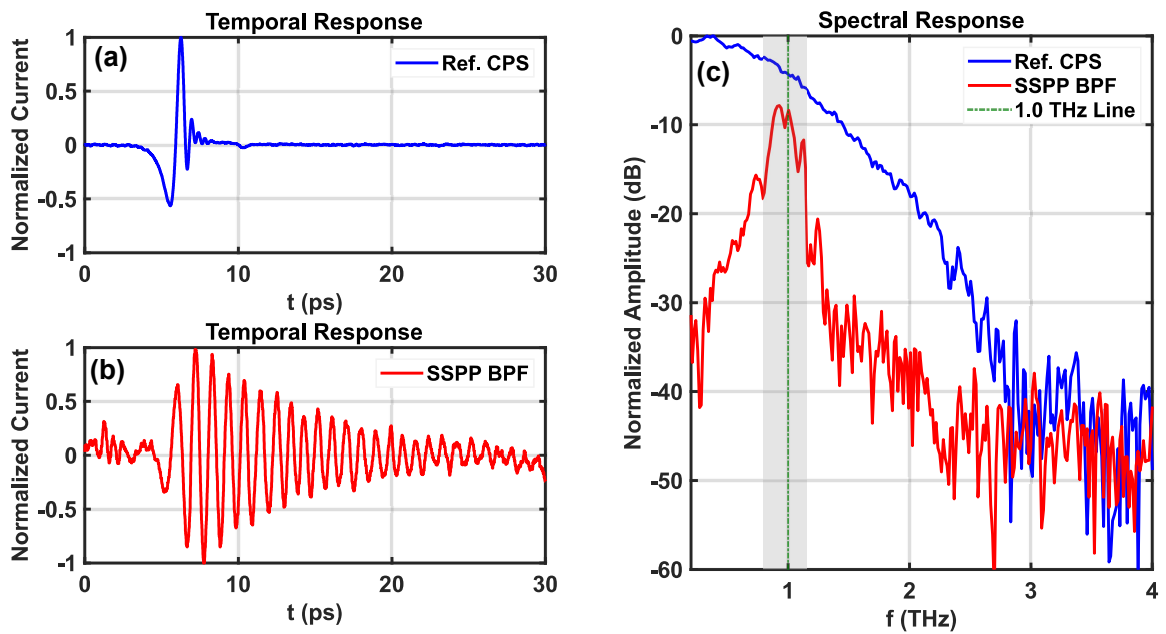


Fig. 9: Measurement results for the proposed SSPP-based BPF and corresponding reference CPS

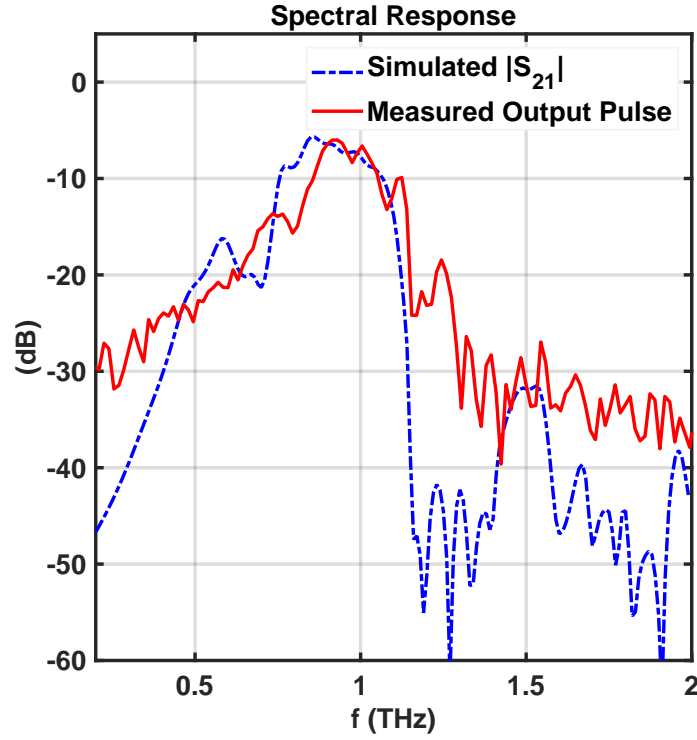


Fig. 10: Simulated $|S_{21}|$ vs normalized amplitude output measured pulse (in dB) for the structure with $H_n = 42 \mu\text{m}$.

aligned with simulations. Notably, the integration of a single-conductor SSPP with a dual-conductor CPS feedline represents a pioneering approach. The guided-wave transmission of the THz signal was enabled by the use of a thin $1 \mu\text{m}$ Silicon Nitride membrane to mitigate loss and dispersion within the THz range. This study holds promise for a wide range of applications in next-generation communication systems, interconnects, and material sensing, highlighting the significance of planar SSPP structures in advancing THz technologies.

Acknowledgments

This work was supported by an NSERC Discovery Grant. The authors thank 4D LABS at Simon Fraser University for the fabrication of the CPS waveguides and the thin membrane, and also the Center for Advanced Materials and Related Technology (CAMTEC) at the University of Victoria for providing Nanofab facilities for the fabrication of the PCS devices.

Funding This work was supported by the Natural Sciences and Engineering Research Council of Canada (NSERC) (RGPIN-2022-03277).

Availability of data and materials Data supporting the findings of this study are available from the corresponding author L.S. on reasonable request.

Declarations

Ethical Approval Not applicable.

Competing Interests The authors declare no competing interests.

References

1. J. B. Pendry, L. Martín-Moreno, and F. J. Garcia-Vidal. Mimicking surface plasmons with structured surfaces. *Science*, 305(5685):847–848, 2004.
2. F. J. Garcia-Vidal, L. Martín-Moreno, and J. B. Pendry. Surfaces with holes in them: new plasmonic metamaterials. *Journal of Optics A: Pure and Applied Optics*, 7(2):S97, 2005.
3. Wen Xuan Tang, Hao Chi Zhang, Hui Feng Ma, Wei Xiang Jiang, and Tie Jun Cui. Concept, theory, design, and applications of spoof surface plasmon polaritons at microwave frequencies. *Advanced Optical Materials*, 7(1):1800421, 2019.
4. Stefan A Maier et al. *Plasmonics: fundamentals and applications*, volume 1. Springer, 2007.
5. Paloma Arroyo Huidobro, Antonio I. Fernández-Domínguez, John B. Pendry, Luis Martín-Moreno, and Francisco J. Garcia-Vidal. *Spoof Surface Plasmon Metamaterials*. Elements in Emerging Theories and Technologies in Metamaterials. Cambridge University Press, 2018.
6. H. F. Ma, X. Shen, Q. Cheng, W. X. Jiang, and T. J. Cui. Broadband and high-efficiency conversion from guided waves to spoof surface plasmon polaritons. *Laser Photonics Rev.*, 8(1):146–151, Jan. 2014.
7. Muhammed Abdullah Unutmaz and Mehmet Unlu. Terahertz Spoof Surface Plasmon Polariton Waveguides: A Comprehensive Model with Experimental Verification. *Scientific Reports*, 9(1):7616, May 2019.
8. M. A. Unutmaz and M. Unlu. Fixed physical length spoof surface plasmon polariton delay lines for a 2-bit phase shifter. *J. Opt. Soc. Am. B*, 37(4):1116–1121, Mar. 2020.
9. Muhammed Abdullah Unutmaz, Gulay Ozsahin, Tuna Abacilar, and Mehmet Unlu. Investigation of the Transitions for Coplanar Waveguide to Terahertz Spoof Surface Plasmon Polariton Waveguides. *IEEE Transactions on Antennas and Propagation*, 70(4):3002–3010, April 2022.
10. Behnam Mazdouri, Mohammad Mahdi Honari, and Rashid Mirzavand. Miniaturized spoof SPPs filter based on multiple resonators or 5G applications. *Scientific Reports*, 11(1):22557, November 2021.
11. Wen Xuan Tang, Hao Chi Zhang, Hui Feng Ma, Wei Xiang Jiang, and Tie Jun Cui. Concept, Theory, Design, and Applications of Spoof Surface Plasmon Polaritons at Microwave Frequencies. *Advanced Optical Materials*, 7(1):1800421, January 2019.
12. Kai-Da Xu, Ying Jiang Guo, and Xianjin Deng. Terahertz broadband spoof surface plasmon polaritons using high-order mode developed from ultra-compact split-ring grooves. *Optics Express*, 27(4):4354, February 2019.
13. Kai-Da Xu, Fengyu Zhang, Yingjiang Guo, Longfang Ye, and Yanhui Liu. Spoof Surface Plasmon Polaritons Based on Balanced Coplanar Stripline Waveguides. *IEEE Photonics Technology Letters*, 32(1):55–58, January 2020.
14. M. Haghghat, T. Darcie, and L. Smith. Demonstration of a terahertz coplanar-strip spoof-surface-plasmon-polariton low-pass filter. *Scientific Reports*, 14, 2024.
15. Ying Jiang Guo, Kai Da Xu, and Xiaohong Tang. Spoof plasmonic waveguide developed from coplanar stripline for strongly confined terahertz propagation and its application in microwave filters. *Optics Express*, 26(8):10589, April 2018.
16. Ying Jiang Guo, Kai Da Xu, Yanhui Liu, and Xiaohong Tang. Novel surface plasmon polariton waveguides with enhanced field confinement for microwave-frequency ultra-wideband bandpass filters. *IEEE Access*, 6:10249–10256, 2018.
17. Jun Wang, Lei Zhao, and Zhang-Cheng Hao. A band-pass filter based on the spoof surface plasmon polaritons and cpw-based coupling structure. *IEEE Access*, 7:35089–35096, 2019.
18. Yiwen Wei, Yongle Wu, Weimin Wang, Leidan Pan, Yuhao Yang, and Yuanan Liu. Double-sided spoof surface plasmon polaritons- line bandpass filter with excellent dual-band filtering and wide upper band suppressions. *IEEE Transactions on Plasma Science*, 48(12):4134–4143, 2020.

19. Yiqun Liu, Kai-Da Xu, Jianxing Li, Ying-Jiang Guo, Anxue Zhang, and Qiang Chen. Millimeter-wave e-plane waveguide bandpass filters based on spoof surface plasmon polaritons. *IEEE Transactions on Microwave Theory and Techniques*, 70(10):4399–4409, 2022.
20. Yinian Feng, Kai-Da Xu, Zhongqian Niu, Bo Zhang, Lujie Liu, and Yong Fan. Ka-band waveguide bandpass filters using double-layer grounded spoof surface plasmon polaritons. *IEEE Transactions on Microwave Theory and Techniques*, pages 1–11, 2024.
21. Ho-Jin Song and Namyoong Lee. Terahertz communications: Challenges in the next decade. *IEEE Transactions on Terahertz Science and Technology*, 12(2):105–117, 2022.
22. Mohsen Haghghat, Thomas Darcie, and Levi Smith. A thz spoof surface plasmon polariton band pass filter for 6g communication applications. In *2024 IEEE Pacific Rim Conference on Communications, Computers and Signal Processing (PACRIM)*, pages 1–4, 2024.
23. Levi Smith and Thomas Darcie. Demonstration of a low-distortion terahertz system-on-chip using a cps waveguide on a thin membrane substrate. *Optics Express*, 27(10):13653–13663, May 2019.
24. Giuseppe Cataldo, James A. Beall, Hsiao-Mei Cho, Brendan McAndrew, Michael D. Niemack, and Edward J. Wollack. Infrared dielectric properties of low-stress silicon nitride. *Optics Letters*, 37(20):4200–4202, Oct 2012.
25. Stefan A. Maier, Steve R. Andrews, L. Martín-Moreno, and F. J. García-Vidal. Terahertz Surface Plasmon-Polariton Propagation and Focusing on Periodically Corrugated Metal Wires. *Physical Review Letters*, 97(17):176805, October 2006.
26. Xiaopeng Shen, Tie Jun Cui, Diego Martin-Cano, and Francisco J. Garcia-Vidal. Conformal surface plasmons propagating on ultrathin and flexible films. *Proceedings of the National Academy of Sciences*, 110(1):40–45, 2013.
27. E. Yablonovitch, D. M. Hwang, T. J. Gmitter, L. T. Florez, and J. P. Harbison. Van der Waals bonding of GaAs epitaxial liftoff films onto arbitrary substrates. *Applied Physics Letters*, 56(24):2419–2421, 06 1990.
28. Walid Gomaa, Levi Smith, Vahid Shiran, and Thomas Darcie. Terahertz low-pass filter based on cascaded resonators formed by CPS bending on a thin membrane. *Optics Express*, 28(21):31967, October 2020.
29. Rubén Darío Velásquez Ríos, Siméon Bikorimana, Muhammad Ali Ummy, Roger Dorsinville, and Sang-Woo Seo. A bow-tie photoconductive antenna using a low-temperature-grown gaas thin-film on a silicon substrate for terahertz wave generation and detection. *Journal of Optics*, 17(12):125802, 2015.